Nonlinear and linearized gray box models of direct-write printing dynamics

Andrej Simeunović and David John Hoelzle
Department of Mechanical and Aerospace Engineering, The Ohio State University, Columbus, Ohio, USA

Abstract

Purpose – The purpose of this study is to develop nonlinear and linearized models of DW printing dynamics that capture the complexity of DW while remaining integrable into control schemes. Control of material metering in extrusion-based additive manufacturing modalities, such as positive displacement direct-write (DW), is critical for manufacturing accuracy. However, in DW, transient flows are poorly controlled due to capacitive pressure dynamics – pressure is stored and slowly released over time from the build material and other compliant system elements, adversely impacting flow rate start-ups and stops. Thus far, modeling of these dynamics has ranged from simplistic, potentially omitting key contributors to the observed phenomena, to highly complex, making usage in control schemes difficult.

Design/methodology/approach – The authors present nonlinear and linearized models that seek to both capture the capacitive and nonlinear resistive fluid elements of DW systems and to pose them as ordinary differential equations for integration into control schemes. The authors validate the theoretical study with experimental flow rate and material measurements across a range of extrusion nozzle sizes and materials. The authors explore the contribution of the system and build material bulk modulus to these dynamics.

Findings – The authors show that all tested models accurately describe the measured dynamics, facilitating ease of integration into future control systems. Additionally, the authors show that system bulk modulus may be substantially reduced through appropriate system design. However, the remaining build material bulk modulus is sufficient to require feedback control for accurate material delivery.

Originality/value – This study presents new nonlinear and linear models for DW printing dynamics. The authors show that linear models are sufficient to describe the dynamics, with small errors between nonlinear and linear models. The authors demonstrate control is necessary for accurate material delivery in DW.

Keywords Modeling, Direct-write, Grey box

Paper type Research paper

1. Introduction

Direct-write (DW) printing (also termed microextrusion, robocasting or micro-robotic deposition) is an additive manufacturing (AM) method whereby the build material is extruded through a nozzle by a mechanical plunger or pressurized air as the nozzle moves in three-dimensional space across a printing platform (Gibson and Stucker, 2015; Cesarano et al., 1998) [Figures 1(a) and 1(b)]. DW is popular because of its simplicity, ability to directly deliver material, ability to create multi-material constructs, and material diversity (Gu, 2015; Deliormanlı and Rahaman, 2012; Hollister, 2005; Bajaj et al., 2014). However, DW systems have capacitive pressure dynamics, which lead to poor deposition control in transient flows. For example, consider the fabrication of simple, two-dimensional shapes using hydroxyapatite (HA) [Figure 1(c)], a DW build material that has been used in the printing of synthetic tissue scaffolds. In both circle and triangle constructs, the slow flowrate transient response leads to a lack of material at the start of constructs and undesirable material at the end

The current issue and full text archive of this journal is available on Emerald Insight at: https://www.emerald.com/insight/1355-2546.htm

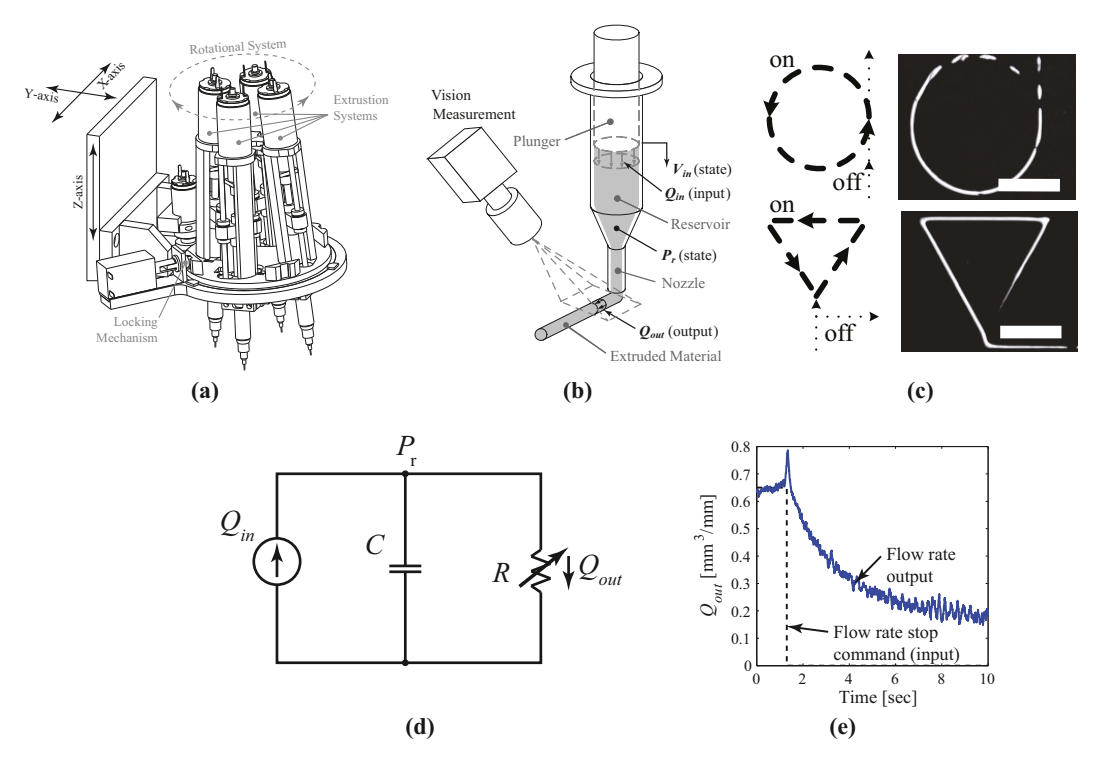


Schematics of the positive displacement DW system used in this paper are shown in Figures 1(a) and 1(b). This system has been previously described in Xie et al. (2016). Using a fluid circuit analogy, the dynamics in the DW system can be described as a reservoir with a fluidic capacitance and nozzle with a nonlinear resistance [Figure 1(d)]. Because the plunger in DW acts upon the inlet of the material reservoir, extrusion pressure, P_r , is transmitted throughout the entire material reservoir and is stored within the build material and other compliant elements of the system, acting as a single capacitive element, C. The viscoplastic behavior of the build material leads to a nonlinear resistance to flow, $R(P_r)$, as pressure is applied. These capacitive and resistive elements lead to transient flow rate responses with an observable, pressure-dependent resistive-capacitive (RC) time constant for typical on or off step inputs [Figure 1(e)]. Note that a normalized volumetric

Support for this research was provided in part by NSF CAREER Award CMMI 1708819 and NSF GRFP Award DGE-1343012. The authors wish to acknowledge Professor Yael Vodovotz and Drs Sravanti Paluri and John Frelka for their training, guidance, and support during rheology testing, and for the usage of rheometers. They acknowledge Ashley Allison Armstrong and Professor Amy J. Wagoner Johnson for providing hydroxyapatite build material for this work. They acknowledge Stephen Bedard for early work on the nonlinear modeling presented here. They acknowledge Kevin Wolf for machining custom reservoir holders.

Received 3 December 2018 Revised 8 November 2019 22 May 2020 Accepted 2 June 2020

Figure 1 DW printing and challenges in DW flow control



Notes: (a) Schematic of DW AM system used in this work. (Image from (Hoelzle *et al.*, 2011). Used with permission from ASME.); (b) Piston-driven DW extruder head in DW system. Volumetric flow rates Q_{in} and Q_{out} are the input and output, respectively. Input volume V_{in} and reservoir pressure P_r are the states. (Image from (Hoelzle *et al.*, 2011). Used with permission from ASME.); (c) DW demonstrates poor transient flow control when printing simple shapes. Scale bars are 5 mm. (Image from (Hoelzle *et al.*, 2008) Used with permission from IEEE.); (d) Fluid circuit analogy of DW dynamics, showing capacitive and nonlinear resistive elements; (e) Q_{out} response for an input flow rate step from steady-state to zero. Fluidic system is characteristic of a first-order RC circuit. Q_{out} requires more than 10 seconds to reach zero

flow rate is used to characterize flow: unit volume per unit length, which provides a measure of the cross-sectional area of material delivered. If not stated explicitly, flow rates in this paper refer to the normalized flow rate.

Modeling of positive displacement DW dynamics in the literature ranges from simplistic, potentially omitting key contributors to the observed phenomena, to highly complex, making their application in control schemes difficult. Nomenclature for DW modeling is presented in Table 1. Early DW modeling in the literature (Morissette et al., 2000) used a simple, algebraic conservation of volume model, tying the flowrates to the nozzle velocity and radius, $Q = Q_{in} = Q_{out} =$ $\pi R^2 v$. From Figures 1(c) and 1(e), it is clear that this model is inaccurate in the transient. Hoelzle et al. (2008) used a more complex approach by modeling DW build materials as compressible and pseudoplastic, which led to the formulation in equation (1). Local linearization about nominal reservoir volume and pressure produced the first-order approximation in equations (2) and (3). With this approach, the outflow response to plunger velocity includes a simple delay, λ , to capture the time taken to exceed the material yield stress. While this model proved effective for control system integration, it did not accurately represent low flowrate transient modes as it does not model the contribution of material yield stress. Accordingly, time-delay fitting factor $\lambda = 0$ when operating above the yield stress and $\lambda > 0$ when operating below the yield stress:

$$\frac{V_0 - V_{in}}{\beta} \frac{nC_2}{C_1} \left(\frac{P_r}{C_2}\right)^{1 - 1/n} \dot{Q}_{out} + Q_{out} = A_p \dot{\delta}$$
 (1)

$$Q_{out}/\dot{\delta}(s) = \frac{A_p}{Ts+1}e^{-\lambda s}$$
 (2)

$$T = \frac{V_0 - \overline{V}_{in}}{\beta} \frac{nC_2}{C_1} \left(\frac{\overline{P}_r}{C_2}\right)^{1 - 1/n} \tag{3}$$

Li et al. (2013a) and (2013b) used a more complex model by assuming yield-pseudoplastic build materials and a complex constitutive model for yield-pseudoplastic fluids where apparent viscosity is described by equation (4). A Navier–Stokes-based framework was used for derivation of build material extrusion response and build material was assumed compressible with air bubbles present. This work focused on extrusion of aqueous-based ceramic build materials, formulated in terms of extrusion force, F_{ram} ,

Table 1 Nomenclature for dynamic modeling parameters

Symbol	Parameter		
$\overline{A_p}$	Plunger Cross-sectional Area		
β -(30 + 1)/2	Bulk Modulus		
$C_1 = \frac{\pi n R^{(3n+1)/n}}{3n+1}$	Consolidated Constant 1		
$C_2 = 2 mL$	Consolidated Constant 2		
$\dot{\delta}$	Plunger Velocity		
η	Apparent Viscosity		
F _{ram}	Extrusion Force		
F_f	Plunger/Barrel Friction Force		
Ϋ́	Shear Rate		
$\dot{\gamma_c}$	Critical Shear Rate		
L	Nozzle Length		
I_0	Nominal Air Layer Thickness		
I_p	Build Material Length in Nozzle		
m	Flow Consistency Index		
n	Flow Behavior Index		
P	Pressure Function		
P _{atm}	Atmospheric Pressure		
p_c	Compressible Material Pressure		
P_r	Reservoir Pressure		
\overline{P}_r	Reservoir Pressure Operating Point		
Q _{in}	Input Volumetric Flow Rate		
Q _{out}	Output Volumetric Flow Rate		
R	Nozzle Radius		
au	Shear Stress		
$ au_0$	Yield Stress		
$ au_{W}$	Wall Shear Stress		
V	Nozzle Tip Velocity		
V_0	Initial Reservoir Volume		
V _{in}	Input Volume		
\overline{V}_{in}	Input Volume Operating Point		

resulting in a first-order nonlinear governing equation [equation (5)]:

$$\eta = \begin{cases}
\frac{\tau_0}{|\dot{\gamma}|} + m \frac{|\dot{\gamma}|^{n-1}}{\dot{\gamma}_c^{n-1}} & \text{if } |\dot{\gamma}| \ge \dot{\gamma_c} \\
\left[\frac{2\tau_0}{\dot{\gamma_c}} + m(2-n) \right] + \left[\frac{m(n-1)}{\dot{\gamma_c}} - \frac{\tau_0}{\dot{\gamma}_c^2} \right] |\dot{\gamma}| & \text{if } |\dot{\gamma}| < \dot{\gamma}_c
\end{cases}$$

$$\dot{F}_{ram}(t) = \frac{\left[F_{ram}(t) - F_f \operatorname{sgn}(\dot{\delta}) + A_p p_{atm} \right]^2}{A_p p_c(0) l_0} \left[\dot{\delta}(t) - P^{-1} \right]$$

$$\left[\frac{F_{ram}(t) - F_f \operatorname{sgn}(\dot{\delta})}{A_p l_p(t)} \right] \qquad (5)$$

Li's approach resulted in an absolute per cent error between experimental and simulated responses of 6.3% in a single extruder system, demonstrating accurate modeling of the transient and steady-state dynamics of extrusion of this subset of DW build materials, including the very complex case of air bubbles traveling through the material reservoir and exiting the nozzle. However, the implementation of this model in control architectures faces challenges because of its complexity. Like

Hoelzle *et al.*, Li *et al.* found that for common printing modes, such as when the extrusion force is sufficiently large, the dynamic response is dominated by a first-order response. Additionally, air bubbles can be potentially eliminated from the material reservoir entirely through appropriate system and process design. Thus, the complexity of the Li *et al.* model may be unnecessary to capture the majority of the contributors to the observed phenomena of DW printing.

The objective of this work is to synthesize a lumpedparameter gray-box model of positive displacement DW of yield-pseudoplastic fluids and to validate the model through extrusion experiments. We seek to model the dominant capacitive elements of DW dynamics and for this model to be directly integrable into nonlinear and linear control schemes. This is accomplished by developing a complex, nonlinear base model, which is then linearized into Wiener (Wills et al., 2013; Schetzen, 1980) and linear models (Section 2). The Wiener model is the middle ground between the nonlinear and linear models, as it provides linear state equations while preserving the nonlinear relationship between state and output. We validate our theoretical work with experimental measurements in a DW system, including extrusion of materials that span a diverse set of DW applications - tissue engineering (HA), electronics fabrication [solder paste (SP)] and food science [toothpaste (TP)] - through two different nozzle sizes (Sections 3 and 4). The paper concludes with discussions on the implications of the compliance innate to the build materials and the need for feedback control (Section 5).

2. Dynamics of direct-write printing

DW operates by leveraging the material properties of non-Newtonian fluids. The build material, typically a suspended ceramic or polymeric slurry or paste, is located in a reservoir upstream of the nozzle. DW build materials are yield-pseudoplastic – shear-thinning non-Newtonian fluids with finite yield stress [Figure 2(a)]. Nominally, build material is solid in the reservoir, but by applying shear stress that exceeds the yield stress, the apparent viscosity drops and build material is extruded through the nozzle [Figure 1(b)]. When shear stress drops below the yield stress on the build platform, the deposited build material sets and holds its shape, facilitating the building of three-dimensional constructs. Typically, post-processing procedures, such as high-temperature sintering, are applied to the solidified part to achieve desired material properties.

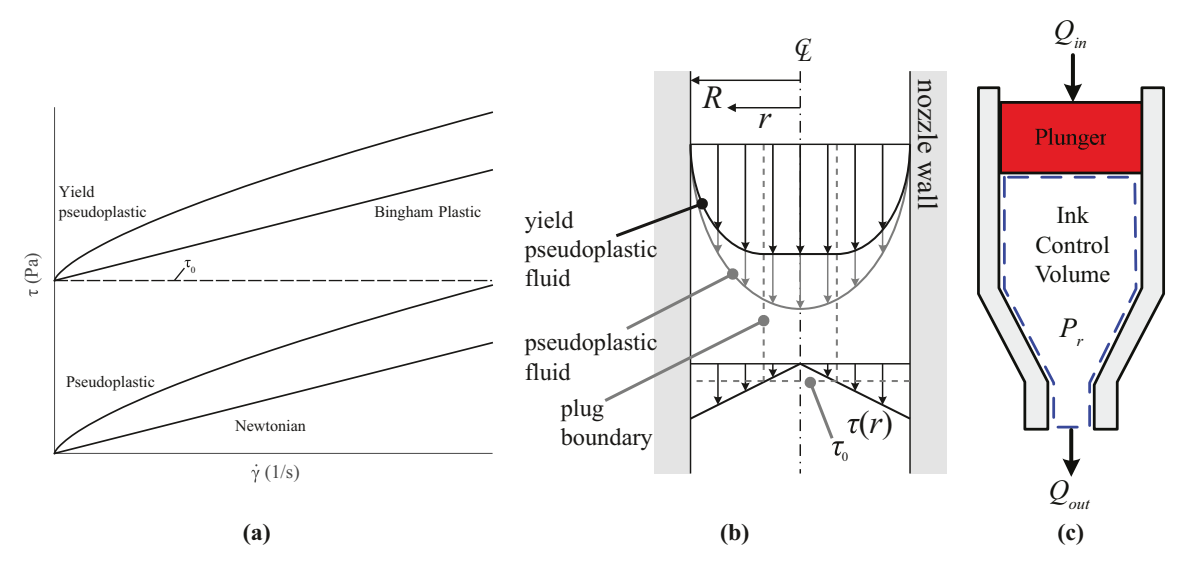
2.1 Base nonlinear model

We focus our analysis on two domains, namely, compressible flow through the reservoir and non-Newtonian flow through the nozzle. For standard DW systems, the reservoir has a radius that is an order of magnitude greater than the nozzle radius and a volume that is four orders of magnitude greater than nozzle volume; given the \propto R⁻⁴ relationship between fluidic resistance and radius and \propto V relationship between volume and fluidic capacitance, the reservoir is modeled as a capacitor and the nozzle is modeled as a resistor [Figure 1(d)].

2.1.1 Nozzle domain

We assume an adiabatic process with laminar flow of yieldpseudoplastic fluids. Nomenclature for dynamic modeling is

Figure 2 Schematics for model development



Notes: (a) Yield-pseudoplastic fluids exhibit both shear thinning and a finite yield stress (τ_0) which must be overcome for flow to begin. Motivated by figure in (Chhabra and Richardson, 2008); (b) velocity and stress distributions of pseudoplastic and yield-pseudoplastic fluid flows in a nozzle. Yield-pseudoplastic flow has solid plug at the center surrounded by shear-thinning outer layer at the nozzle wall. Shear stress is maximum at the wall and zero at the center of the plug. Motivated by figure in (Chhabra and Richardson, 2008); (c) Control volume of build material in reservoir. Figure modified from (Hoelzle *et al.*, 2008)

presented in Table 1. We represent the yield-pseudoplastic build materials with the Herschel-Bulkley constitutive equation:

$$\tau = \tau_0 + m\dot{\gamma}^{\rm n} \tag{6}$$

where for a given shear rate $\dot{\gamma}$, the one-dimensional shear stress, τ , is defined by the yield stress τ_0 , the fluid consistency index or coefficient m and the flow behavior index or coefficient n (Chhabra and Richardson, 2008) [Figure 2(a)]. The flow behavior index quantifies the

response of the apparent viscosity to shear-rate, with n > 1 corresponding to shear-thickening behavior, n < 1 corresponding to shear-thinning behavior, and n = 1 being Newtonian. Yield-pseudoplastic fluids for DW will always have n < 1. The three Herschel-Bulkley parameters can be measured by standard flow sweep rheology measurements, which we describe in Section 3.2. The nozzle domain is modeled as yield-pseudoplastic fluid flow through a pipe [Figure 2(b)], which is governed by:

$$Q_{out} = \begin{cases} \pi R^3 n \left(\frac{\tau_{\varpi}}{m}\right)^{1/n} (1-\phi)^{(n+1)/n} \left[\frac{(1-\phi)^2}{3n+1} + \frac{2\phi(1-\phi)}{2n+1} + \frac{\phi^2}{n+1} \right] & \text{for } \phi \leq 1 \\ 0 & \text{for } \phi > 1 \end{cases}$$
(7)

where $\phi=\frac{\tau_0}{\tau_w}$, $\tau_w=\left(\frac{-P_r}{L}\right)\frac{R}{2}$ and which is derived in (Chhabra and Richardson, 2008).

2.1.2 Reservoir domain

The reservoir domain is modeled with the control volume in Figure 2(c), where the flow-pressure relationship is governed by:

$$\dot{P}_r = \frac{\beta}{V_0 - V_{in}} (Q_{in} - Q_{out}) \tag{8}$$

$$\dot{V}_{in} = Q_{in} \tag{9}$$

which are derived in (Hoelzle et al., 2008).

2.2 Nonlinear model summary

The base nonlinear model combines the equations for the reservoir and nozzle domains [equations (7)-(9)] to relate the flow rate at the reservoir inlet to the flow rate at the nozzle outlet. The system describing the reservoir [equations (8) and (9)] is solved to find the pressure in the material reservoir. Reservoir pressure is used to find the wall shear stress, τ_w , which allows for the direct calculation of output flow rate from the nozzle using equation (7).

All model parameters except the bulk modulus, β , are known geometric parameters or identified with rheological experiments (Section 3.2). β is an effective parameter that lumps together the innate bulk modulus of the build material with an effective bulk

modulus of the reservoir structure. As the exact contribution of the reservoir and build material to the bulk modulus is unknown, β must be determined experimentally for each material. Thus, the base nonlinear model is a gray box model with one fitting parameter.

2.3 Wiener model and linear model

The Wiener and linear models leverage a linearization of the capacitive state dynamics, equations (8) and (9):

$$\begin{bmatrix} \frac{d\hat{V}_{in}}{dt} \\ \frac{d\hat{P}_r}{dt} \end{bmatrix} = \begin{bmatrix} 0 & 0 \\ 0 & A_{2,2} \end{bmatrix} \begin{bmatrix} \hat{V}_{in} \\ \hat{P}_r \end{bmatrix} + \begin{bmatrix} 1 \\ \frac{\beta}{V_0 - \overline{V}_{in}} \end{bmatrix} \hat{Q}_{in}$$

where term $A_{2,2}$ is given by:

$$A_{2,2} = -\frac{\beta}{V_0 - \overline{V}_{in}} \frac{\partial Q_{out}}{\partial P_r} \bigg|_{P_r = \overline{P}_r}.$$
 (11)

Linearization is performed about steady-state flow, where flowrate operating points are $\overline{Q}_{in} = \overline{Q}_{out} = \pi R^2 v$ and state operating points \overline{V}_{in} and \overline{P}_r are solutions to the nonlinear model when $\dot{P}_r = 0$. The Wiener model maps the linear states to the output flow rate at the nozzle outlet using equation (7). The linear model uses a linearized form of equation (7), equation (12), to map the states to the output flow rate. Derivations of equations (10)-(12) are presented in the Appendix:

$$\dot{P}_{r} = \frac{\beta}{V_{0} - V_{in}} (Q_{in} - Q_{out}) \tag{12}$$

Note that both the Wiener and linear models are only valid when $\tau_w > \tau_0$ as a flow of the build material only occurs with this relation satisfied. Thus, the pressure term is bounded for all time t such that:

$$P_r(t) \geq P_{r,min} = rac{2L au_0}{R}.$$

In both the Wiener and linear model, the eigenvalues are 0 [because of the integrator in equation (9)] and $A_{2,2}$. Thus, the system time constant becomes $\tau = \frac{1}{A_{2,2}}$, where τ is a fluidic RC time constant that characterizes the pressure response of the system.

3. Experimental methods

We perform two types of experiments, flowrate response and rheology. Flow rate response experiments consist of extruding a simple, single layer construct and measuring output volumetric flow rate over time (Sections 3.2.1 and 3.2.2). We use the experimental data to complete the three models and evaluate their accuracy (Sections 3.2.3 and 3.2.4). Flow rate experiments are performed with different nozzle sizes, build materials, and reservoirs; the details of flow rate experimental configurations are presented in Table 2. Different nozzle sizes and build materials are used to validate the models across a wider range of pressure gradients and material properties, respectively, and together to better represent the diverse set of DW applications in the field. Rheometry experiments are

Table 2 Experimental configurations used for model validation

Exp. config.	Nozzle size	Build material	Reservoir
1	330 <i>µ</i> m	HA	Plastic
2	510 <i>µ</i> m		
3	330 <i>µ</i> m	SP	Plastic
4	510 <i>µ</i> m		
5	330 <i>µ</i> m	TP	Plastic
6	510 <i>µ</i> m		
7	330 <i>µ</i> m	TP	Glass
8	510 <i>μ</i> m		

carried out for each tested material and consist of standard flow sweeps, where shear stress is measured as a function of shear rate (Section 3.2.5). Parameters for the Herschel–Bulkley constitutive equation are determined by fitting equation (6) to the flow sweep data.

For flow rate experiments, we report per cent error between models and experiments to quantify model accuracy. We choose an acceptability threshold for per cent error of \leq 15% due to the difficulty of accurately measuring flow rate using a machine vision analysis procedure. We report changes in bulk modulus β to quantify the reduction of compliance from using a non-compliant glass reservoir in place of the compliant plastic reservoir typically used in the DW system. Note that only the toothpaste build material is extruded in glass reservoirs. The suspended particles in HA and SP fill the microstructure of the ground glass walls, causing the plunger to seize during deposition. For rheology experiments, we report Herschel–Bulkley parameters and R^2 values for goodness of fit evaluation.

3.1 Direct-write system

The DW system consists of a custom extruder assembly attached to an X-Y-Z gantry system (X-Y: Aerotech ANT130XY, Z: ANT130LZ) (Figure 3). A high-magnification camera (Basler acA1300-30 μ m) is used for the machine vision analysis described in Section 3.2.2. The positions and velocities of the extruder plunger and gantry system are feedback-controlled with high accuracy and do not contribute to the dynamics. The DW system is controlled with a computer running a custom control program and a graphical user interface in Matlab Simulink.

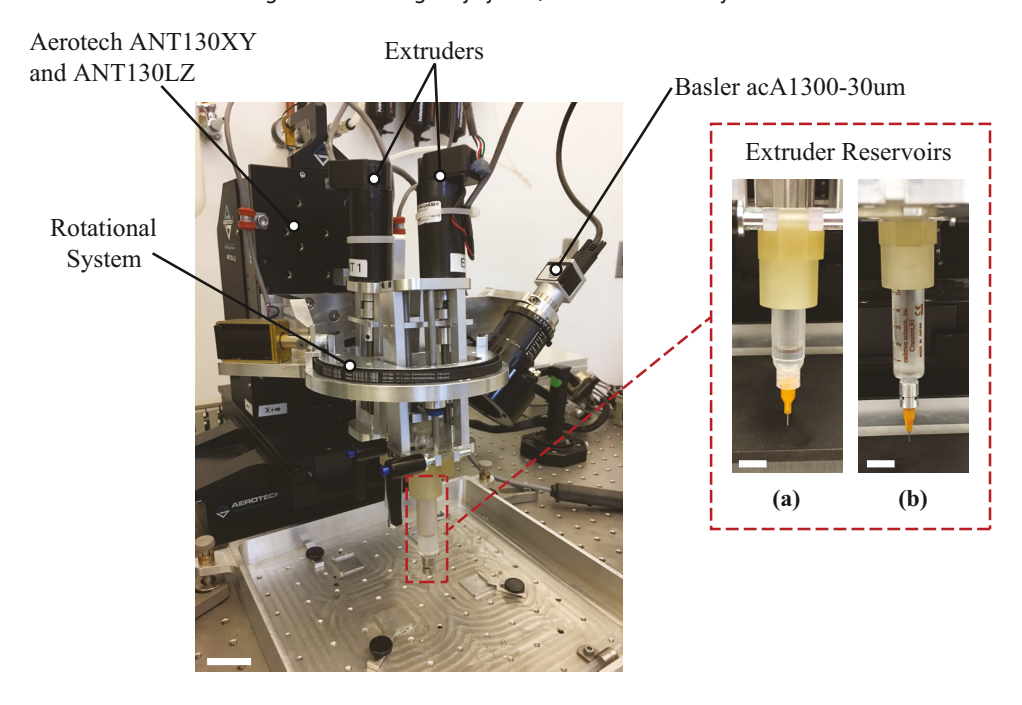
Each extruder subsystem – consisting of a reservoir, plunger, motor with lead screw, and nozzle – is identical. Plastic (Nordson EFD Optimum®) and glass (Cadence Science Perfektum®) syringes are used for reservoirs (subfigure of Figure 3) and blunt-tipped needles with a 510 μ m inner diameter (Nordson EFD 7005005) and 330 μ m inner diameter (Nordsen EFD 7018302) are used for nozzles.

3.2 Methods

3.2.1 Flow rate experiments

Material is extruded in a U-shape for each flow rate experiment [Figure 4(a)]. The first portion of the extrusion path is sufficiently long for flow to transition from transient to steady-state. Steady-state flow continues until 2 s after the second turn in the extrusion path, at which point the input flow command steps down from steady-state $(Q_{in} = \overline{Q}_{in})$ to zero $(Q_{in} = 0)$ and the resulting transient output flow rate over time is used for model validation.

Figure 3 DW system consists of Aerotech orthogonal three-axis gantry system, custom rotational system and custom extruders. The scale bar is 25 mm



Notes: (a) Compliant, plastic reservoirs; (b) non-compliant, glass reservoirs are used in the DW system. Scale bars are 10 mm

Nozzle velocity, v=5 mm/s, is the same for both 330 μm and 510 μm nozzle experiments. However, the output volumetric flow rate at steady-state, $\overline{Q}_{out}=\pi R^2 v$, will be different for the two nozzle configurations because of differing nozzle radii. The high-magnification camera is attached to the end effector and moves with the extrusion system as printing occurs on the printing platform. The camera is focused at the tip of the nozzle and records the entire deposition process, which is converted to measurements of flow rate over time using the machine vision analysis described in Section 3.2.2. The deposition procedure is repeated a minimum of 10 times; for HA and TP, 10 trials were averaged, while for SP, 15 trials were averaged because of the increased noise observed in SP data.

3.2.2 Machine vision analysis

The U-shape deposition process is recorded using an f/8 aperture and 65 ms exposure time at 15.4 frames per second. A video processing script [Video_Processing_CF.m, Figure 4(b)] takes .avi video files as inputs and outputs volumetric flow rate over time data. The script identifies the first frame of motion using a standard motion detection algorithm (Thresholded Frame Difference (Martinez-Martin and del Pobil, 2012), Movement.m) and compiles a sequence of frames from this starting point. The first frame of interest, 1.5 s before the input flow rate step down command, is identified. At this frame, the user defines the region of interest (ROI) with a rectangular mask [Figure 4(c)]. The remaining frames are converted to a sequence of binary images based on the defined ROI [inset of Figure 4(c)]. We assume that the extruded fluid is a filament with the cross-section shown in Figure 4(d); this assumption is

supported by (Cesarano *et al.*, 1998). Then the width of extruded filament, *W*, in each binary image is measured and used to calculate the normalized volumetric flow rate with:

$$Q_{out} = egin{cases} rac{\pi}{4} \, W^2 & ext{for} & 0 \leq W \leq h \ & rac{1}{2} \, heta \, W^2 + rac{1}{2} \, h^2 rac{1}{ an \, heta} & ext{for} & W > h \end{cases}$$

where h is the standoff height between the nozzle and the substrate and $\theta = \sin^{-1}\left(\frac{2h}{W}\right)$.

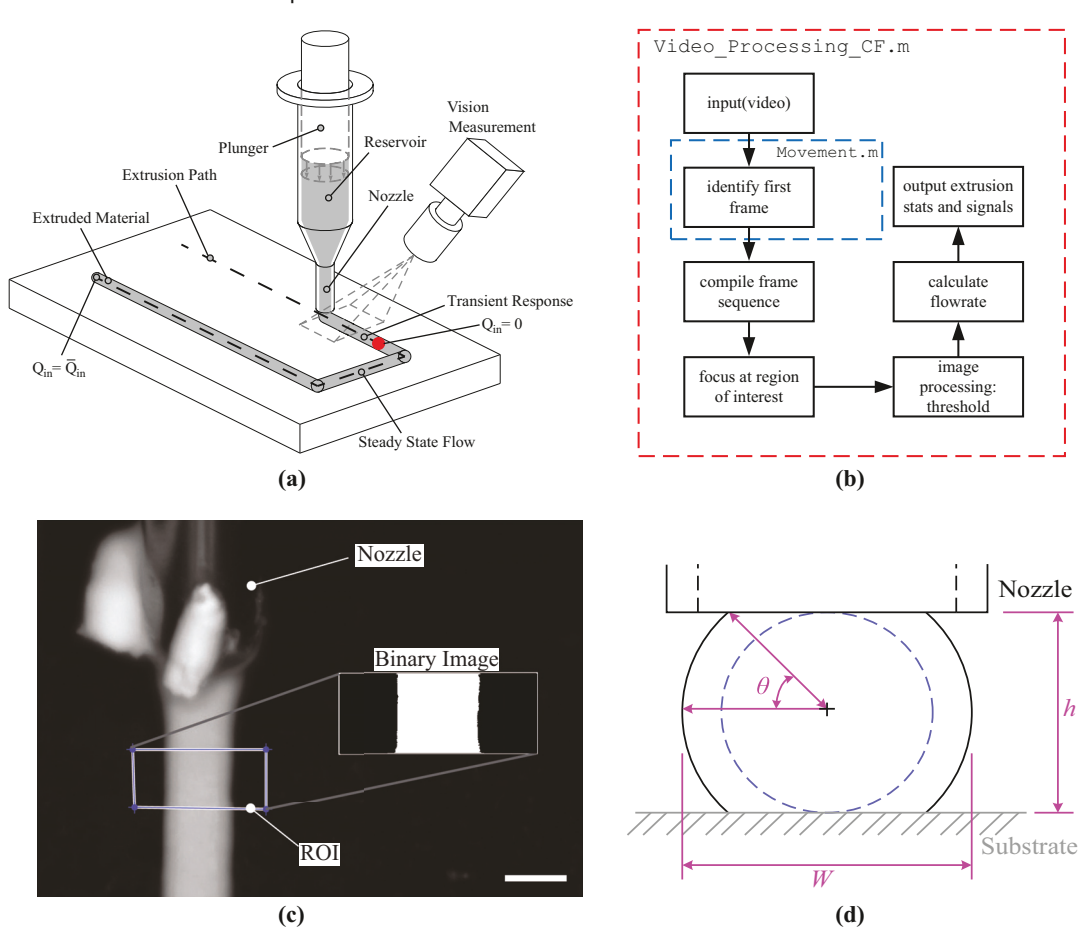
3.2.3 β selection

The pseudo-code in Algorithm 1 describes the selection procedure for unknown bulk modulus term, β . β is determined by minimizing E_{NMS} , which is the normalized mean square error between the nonlinear model volumetric flow rate simulation, $Q_{out,nm}$, and the experimental volumetric flow rate data, $Q_{out,exp}$. Data set $Q_{out,exp}(t,k)$ is the average signal in time across all experimental trials of a given experimental configuration. For a given material, each tested β value is used to run a simulation of the nonlinear model in both 330 μ m and 510 μ m configurations. The normalized mean square error (Lines 11 and 12) is found with:

$$E_{NMS}(\beta, k) = \frac{\|Q_{out,exp}(t, k) - Q_{out,nm}(t, \beta, k)^2\|}{\|Q_{out,exp}(t, k) - \text{mean}(Q_{out,exp}(t, k))^2\|} \quad \text{for} \quad k = 1, 2,$$
(13)

where $\|\cdot\|$ denotes the Euclidean norm, t is the time index, β is the bulk modulus index, and k is the nozzle size index

Figure 4 Details of the volumetric flow rate experiments



Notes: (a) Material is extruded in U-shape ($Q_{in} = \pi R^2 \nu$ before input flow command steps down to zero ($Q_{in} = 0$); (b) script Video_Processing_CF.m converts video inputs to output volumetric flow rate over time data; (c) the video processing algorithm analyses the filament width in a user-defined region of interest (ROI). Scale bar is 250 μ m. Inset: Frames of interest are converted to a sequence of binary images based on the defined ROI; (d) assumed cross-section of extruded build material for volumetric flow rate calculations

corresponding to 330 μ m (k = 1) and 510 μ m (k = 2) data sets. The resulting normalized errors between the simulation and data, equation (13), are averaged to find a scalar error term as a function of β , Line 13; a normalized error is chosen for optimization so that 330 μ m and 510 μ m errors contribute equally. The minimization of the averaged array (Line 15) produces a single, optimal β for each material.

3.2.4 Model errors

To calculate the deviation of models from experimental data, the per cent error is found using:

$$\%Error(t) = \left| \frac{(Q_{out})_{exp} - (Q_{out})_{model}}{(Q_{out})_{exp}} \right| * 100$$
 (14)

where $(Q_{out})_{exp}$ and $(Q_{out})_{model}$ correspond to the experimental and model volumetric flow rate data for a chosen material, nozzle, and model type. Equation (14) results in an array of per cent error at each time step; this array is averaged over time to produce a single per cent error term for the given experimental configuration.

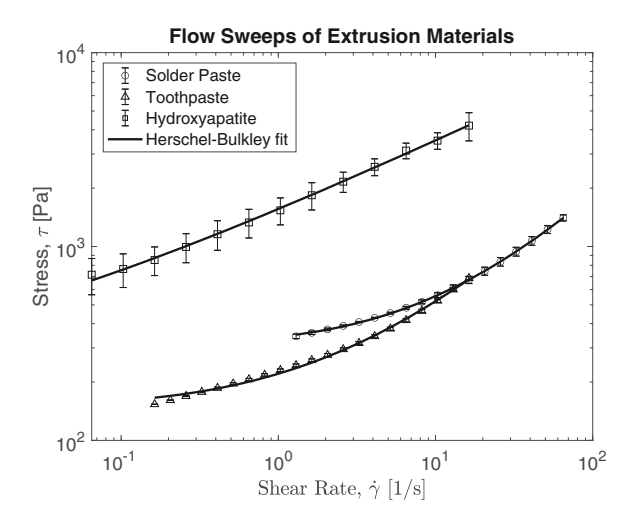
```
Algorithm 1: β Selection
  \begin{array}{ll} \mathbf{1} & \overline{\text{function findBeta}} \left(Q_{out,exp}\left(t,1\right),Q_{out,exp}\left(t,2\right)\right) \\ \mathbf{Input} & : 330\mu\text{m} \; Q_{out,exp} \; \text{data:} \; Q_{out,exp}\left(t,1\right), 510\mu\text{m} \; Q_{out,exp} \; \text{data:} \; Q_{out,exp}\left(t,2\right) \end{array} 
      Output: \beta
 2 \ cont = 1 \ (Condition for while loop)
     while cont = 1 do
            define: a, b, step \ (\beta \text{ lower bound, upper bound, step size})
             \beta_{test}(i) = a : step : b
            for i = 1: length(\beta_{test}) do
                  calculate: Q_{out,nm}\left(t,\beta_{test}(i),1\right)
                   calculate: Q_{out,nm}\left(t,\beta_{test}(i),2\right)
                   calculate: E_{NMS}\left(\beta_{test}(i), 1\right)
                  calculate: E_{NMS}(\beta_{test}(i), 2)
                   E_{NMS}(i) = \text{mean} \left( E_{NMS} \left( \beta_{test}(i), 1 \right), E_{NMS} \left( \beta_{test}(i), 2 \right) \right)
11
12
            i_{opt} = \operatorname{argmin} E_{NMS}(i)
13
            \beta = \beta_{test} (i_{opt})
            define: cont
15
16 end
```

3.2.5 Rheometry

Shear stress measurements are recorded for $\dot{\gamma} = 6.5 \times 10^{-2}$ to $6.5 \times 10^2 \text{ s}^{-1}$ the range of possible shear rates in the DW

system, in logarithmic steps with resolution 10 pts/decade at steady-state temperature 25°C using a rheometer (Discovery HR-2, TA Instruments) with 40 mm parallel plate geometry. For HA, the shear rate resolution was 5 pts/decade to prevent evaporation during testing. Steady-state sensing is used: a measurement for a given shear rate is recorded only if three consecutive measurements taken within 120 s do not exceed 5% deviation. Five flow sweeps are captured and averaged

Figure 5 Rheology flow sweeps for extruded materials. Error bars represent one standard deviation



averaged flow sweep is fit to the Herschel–Bulkley model [equation (6)] to determine the three parameters of the constitutive equation for the given material.

together to produce the final flow sweep for each material. The

3.3 Materials

Materials are SP (Nordson RMA-D200 T2, Sn63/Pb37, P/N: 7020311), TP (Colgate Total Whitening) and HA. HA with a concentration of 50% HA powder was formulated using the procedures outlined in (Michna *et al.*, 2005; Hoelzle, 2011).

4. Results

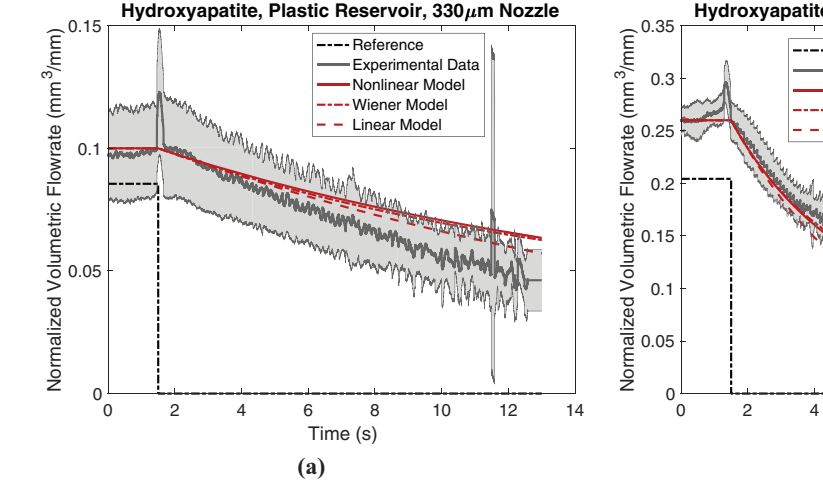
Rheology flow sweeps are presented in Figure 5 and Herschel–Bulkley parameters are presented in Table 3. The fit of the rheology data to equation (6) was excellent, as each data fit had an R^2 value of > 0.99. SP was found to have the highest yield stress, nearly twice that of the TP, which had the lowest. HA was found to be the most viscous, with a fluid consistency index two orders of magnitude higher than SP and TP. Additionally, HA had a much lower flow behavior index than SP and TP, indicating greater shear-thinning behavior.

Experimental and model output volumetric flow rate over time data for each experimental configuration are presented in Figures (6)-(9). As discussed in Section 2.3, the eigenvalues of the Wiener and linear model are 0 and $A_{2,2}$ and the decay of the system is characterized by $\tau = \frac{1}{A_{2,2}}$, where τ is the fluidic RC

Table 3 Herschel–Bulkley parameters for extruded materials

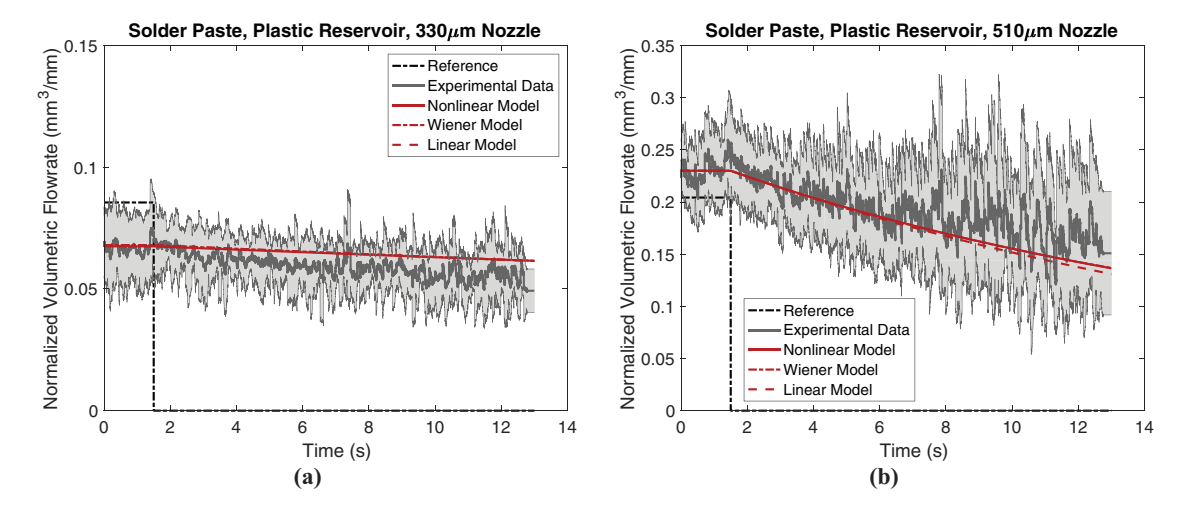
Materials	$ au_0$ [Pa]	m [Pa-s ⁿ]	n	R ²
НА	190.69	1,370.93	0.39	>0.99
SP	299.20	42.03	0.78	>0.99
TP	144.43	76.17	0.70	>0.99

Figure 6 Output volumetric flow rates over time for HA. Shaded regions correspond to one standard deviation



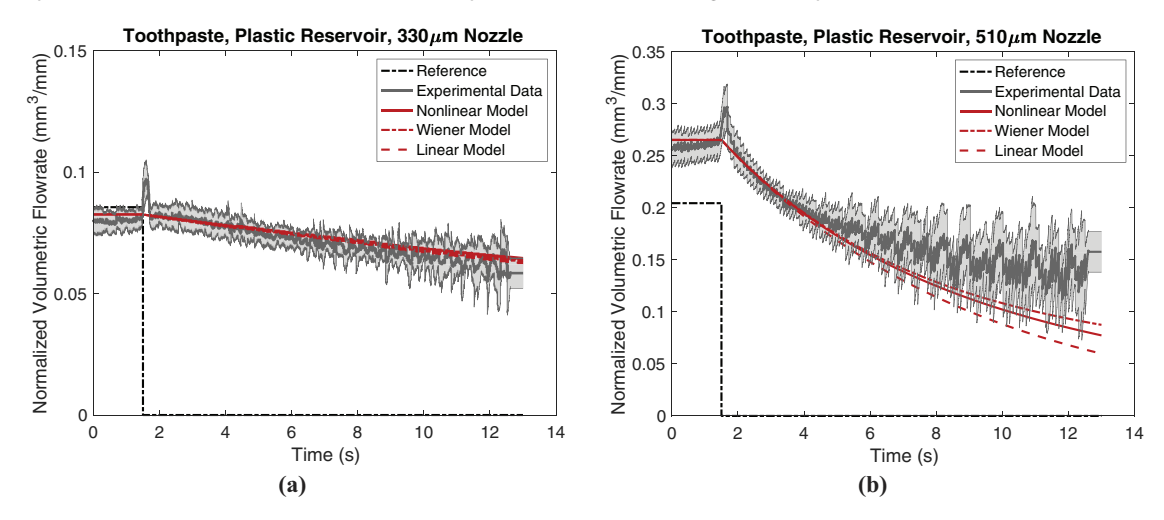
Notes: (a) 330μm nozzle – Experimental configuration 1; (b) 510μm nozzle – Experimental configuration 2

Figure 7 Output volumetric flow rates over time for HA. Shaded regions correspond to one standard deviation



Notes: (a) 330μm nozzle – Experimental configuration 3; (b) 510μm nozzle – Experimental configuration 4

Figure 8 Output volumetric flow rates over time for TP with a plastic reservoir. Shaded regions correspond to one standard deviation



Notes: (a) 330µm nozzle – Experimental configuration 5; (b) 510µm nozzle – Experimental configuration 6

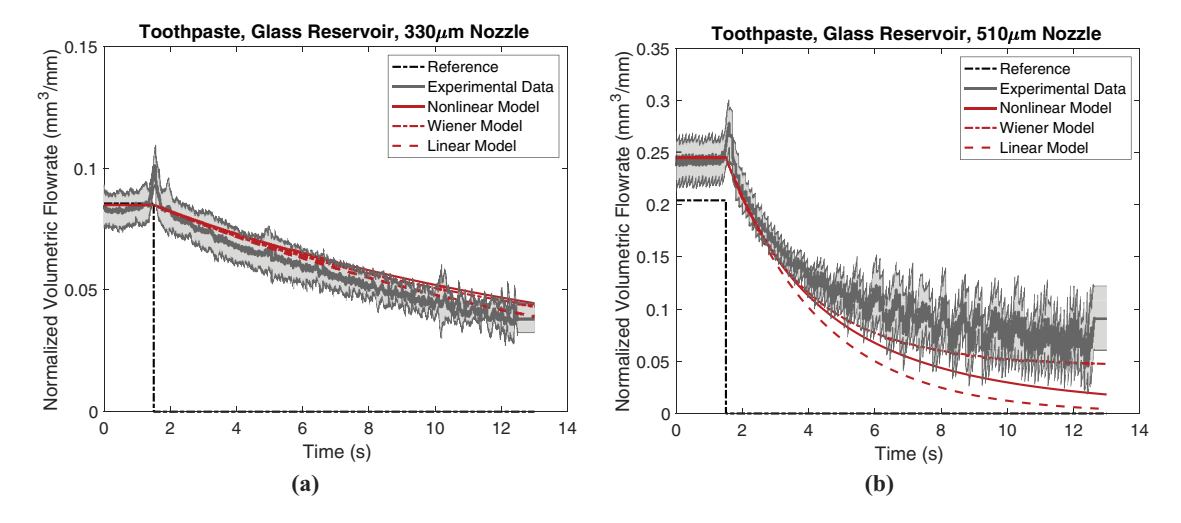
time constant. Thus, with changes in the reservoir wall from compliant plastic to non-compliant glass, we can study changes in system bulk modulus and time constant of the transient response. The output volumetric flow rates of TP printed with different reservoirs are presented in Figure 10, where relevant changes in time constant are highlighted. The identified value for each material and per cent errors of models to experiment are collected in Table 4.

5. Discussion and conclusions

We found good agreement between models and experimental data with a mean per cent error for all experimental configurations across all models of 14.8%, meeting our acceptability threshold of $\leq 15\%$. Looking at configurations across materials, we found mean per cent

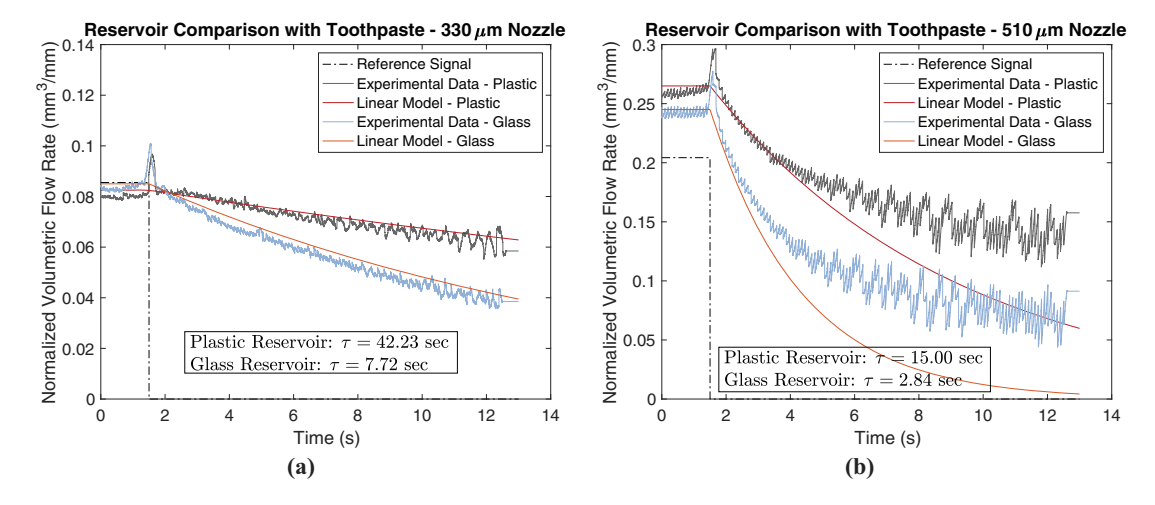
errors of 8.4%, 15.9%, and 18.9%, for SP, TP, and HA, respectively. We suspect the increased number of experimental trials with SP (15 for SP vs. 10 for HA and TP) decreased errors. For all materials, we found a lower mean per cent error for configurations using the 330 µm nozzle (8.3%) compared to the 510 μ m nozzle (21.3%), though this is expected given the noisier experimental data recorded with the larger nozzle size. Near the end of a given flow rate experiment with a 510 μ m nozzle, the material has more difficulty attaching to the printing platform due to lower reservoir pressure, which leads to both increased noise and an offset in the recorded flow rate for the end of the dynamic response. We observed the worst overall per cent errors in the modeling of 510 μ m configurations, with the three highest error configurations having per cent errors ranging from 35%-50%.

Figure 9 Output volumetric flow rates over time for TP with a glass reservoir. Shaded regions correspond to one standard deviation



Notes: (a) 330μm nozzle – Experimental configuration 7; (b) 510μm nozzle – Experimental configuration 8

Figure 10 Comparison of output volumetric flow rates over time for TP with compliant and non-compliant reservoir



Notes: (a) 330µm nozzle; (b) 510µm nozzle

 Table 4 Percent errors of models to experiment. Units are percent if not otherwise specified

Materials		% Error					
		330 μ m nozzle			510 μ m nozzle		
	β [Pa]	Nonlinear	Wiener	Linear	Nonlinear	Wiener	Linear
НА	1.37 × 10 ⁸	14.23	13.13	9.95	23.05	15.21	37.74
SP	6.41×10^6	8.92	9.23	9.20	7.45	7.46	8.30
TP (plastic)	2.04×10^7	4.02	3.35	3.08	16.06	13.88	21.13
TP (glass)	5.67×10^7	10.17	8.41	5.36	35.64	20.24	50.01

Comparing models, we found mean per cent errors of 11.4%, 14.9%, and 18.1%, for the Wiener, nonlinear, and linear models, respectively. These results, for a limited number of studied cases, confirms that using a linearized model such as

the Wiener model instead of a nonlinear model will not incur a high cost in terms of model accuracy loss. Though we found the linear model to be the worst approximation of the experimental data, we found acceptable per cent errors (<10%) for the

majority of experimental configurations (5 of 8). Therefore, for the limited number of studied cases presented here, it is compelling to use a fully linearized model for applications such as control scheme implementations because of its acceptable accuracy and its ease of implementation.

We examined the contribution of the reservoir and build material to the bulk modulus. Eliminating reservoir compliance by using a non-compliant glass reservoir reduced effective system bulk modulus substantially. We found $\beta = 2.04 \times 10^7$ with the compliant (plastic) reservoir and $\beta = 5.67 \times 10^7$ with the non-compliant (glass) reservoir, a per cent change of 177%. However, it is clear that the compliance of the build material is intrinsic, and therefore, positive-displacement DW will always have capacitive dynamics. As seen in Figure 10, an unacceptable amount of material is deposited after a stop command (3.26 μ L for the 330 μ m nozzle and 6.27 μ L for the 510 μ m nozzle).

In future work, we plan to address these dynamics with feedback control using the linear model presented in this work. As real-time flow rate sensors for the μ L volumes that are delivered by DW systems of this type are not yet realized, we feel the most direct way to implement feedback controllers for material delivery is to control reservoir pressure. Other feedback control approaches have shown promise in the literature. Zhao et al. (2010) showed good tracking performance of extrusion force using a feedback control system. More commonly, feedforward methods are used (Han and Jafari, 2007; Hoelzle et al., 2011); however, the system nonlinearity in state V_{in} results in a time-constant that is continually changing as more material is expelled, making model-based feedforward control tools less effective. We plan to explore these challenges in controller design in simulation and then hardware implementation in future work. The current work provides the platform for understanding these problems and the tools to address them.

References

- Bajaj, P., Schweller, R.M., Khademhosseini, A., West, J.L. and Bashir, R. (2014), "3D biofabrication strategies for tissue engineering and regenerative medicine", *Annual Review of Biomedical Engineering*, Vol. 16 No. 1, pp. 247-276.
- Cesarano III, J., Segalman, R. and Calvert, P. (1998), "Robocasting provides moldless fabrication from slurry deposition", *Ceramic Industry*, Vol. 148 No. 4, pp. 94-102.
- Chhabra, R. and Richardson, J. (2008), Non-Newtonian Flow and Applied Rheology: Engineering Applications Second Edition, 2nd ed., Elsevier Ltd. Oxford.
- Deliormanlı, A. and Rahaman, M. (2012), "Direct-write assembly of silicate and borate bioactive glass scaffolds for bone repair", *Journal of the European Ceramic Society*, Vol. 32 No. 14, pp. 3637-3646.
- Gibson, I., Rosen, D. and Stucker, B. (2015), "Additive manufacturing technologies: 3D printing", Rapid Prototyping, and Direct Digital Manufacturing, 2nd ed., Springer, New York, NY.
- Gu, D. (2015), Laser Additive Manufacturing of High-Performance Materials, 1st ed., Springer, New York, NY.

- Han, W. and Jafari, M.A. (2007), "Coordination control of positioning and deposition in layered manufacturing", *IEEE Transactions on Industrial Electronics*, Vol. 54 No. 1, pp. 651-659.
- Hoelzle, D.J. (2011), "Flexible adaptation of iterative learning control with applications to synthetic bone graft manufacturing", Dissertation, the University of Illinois at Urbana-Champaign.
- Hoelzle, D.J., Alleyne, A.G. and Wagoner Johnson, A.J. (2011), "Basis task approach to iterative learning control with applications to a micro-robotic deposition", *IEEE Transactions on Control Systems Technology*, Vol. 19 No. 5, pp. 1138-1148.
- Hoelzle, D.J., Alleyne, A.G. and Wagoner Johnson, A.J. (2008), "Iterative learning control for robotic deposition using machine vision", *American Control Conference*, pp. 4541-4547.
- Hoelzle, D.J., Svientek, S.R., Alleyne, A.G. and Wagoner Johnson, A.J. (2011), "Design and manufacture of combinatorial calcium phosphate bone scaffolds", *Journal of Biomechanical Engineering*, Vol. 133 No. 10, p. 101001.
- Hollister, S.J. (2005), "Porous scaffold design for tissue engineering", *Nature Materials*, Vol. 4 No. 7, pp. 518-524.
- Li, M., Tang, L., Landers, R.G. and Leu, M.C. (2013a),
 "Extrusion process modeling for aqueous-based ceramic pastes
 part 1: constitutive model", *Journal of Manufacturing Science and Engineering*, Vol. 135 No. 5, pp. 51 008–1-51 008–7.
- Li, M., Tang, L., Landers, R.G. and Leu, M.C. (2013b), "Extrusion process modeling for aqueous-based ceramic pastes part 2: experimental verification", *Journal of Manufacturing Science and Engineering*, Vol. 135 No. 5, pp. 51 009–1-051 009–7.
- Martinez-Martin, E. and del Pobil, A.P. (2012), *Robust Motion Detection in Real-Life Scenarios*, 1st ed., Springer, New York, NY.
- Michna, S., Wu, W. and Lewis, J.A. (2005), "Concentrated hydroxyapatite inks for direct-write assembly of 3-D periodic scaffolds", *Biomaterials*, Vol. 26 No. 28, pp. 5632-5639.
- Morissette, S.L., Lewis, J.A., Cesarano III, J., Dimos, D.B. and Baer, T. (2000), "Solid freeform fabrication of aqueous alumina poly(vinyl alcohol) gelcasting suspensions", *Journal of the American Ceramic Society*, Vol. 83 No. 10, pp. 2409-2416.
- Schetzen, M. (1980), The Volterra and Wiener Theories of Nonlinear Systems, 1st ed., Wiley, New York, NY.
- Wills, A., Schön, T.B., Ljung, L. and Ninness, B. (2013), "Identification of Hammerstein-Wiener models", *Automatica*, Vol. 49 No. 1, pp. 70-81.
- Xie, Y., Rustom, L.E., McDermott, A.M., Boerckel, J.D., Johnson, A.J.W., Alleyne, A.G. and Hoelzle, D.J. (2016), "Net shape fabrication of calcium phosphate scaffolds with multiple material domains", *Biofabrication*, Vol. 8 No. 1, p. 015005.
- Zhao, X., Landers, R.G. and Leu, M.C. (2010), "Adaptive extrusion force control of freeze-form extrusion fabrication processes", *Journal of Manufacturing Science and Engineering*, Vol. 132 No. 6, pp. 64 504–1-064 504–9.

Appendix. Derivation of linear state and output equations

The linearized state-space model for the reservoir domain takes the form

$$\begin{bmatrix} \frac{d(\hat{V}_{in})}{dt} \\ \frac{d(\hat{P}_r)}{dt} \end{bmatrix} = \begin{bmatrix} A_{1,1} & A_{1,2} \\ A_{2,1} & A_{2,2} \end{bmatrix} \begin{bmatrix} \hat{V}_{in} \\ \hat{P}_r \end{bmatrix} + \begin{bmatrix} B_1 \\ B_2 \end{bmatrix} \hat{Q}_{in}.$$

Linearizing equation (9) using $V_{in} = \hat{V}_{in} + \overline{V}_{in}$, we find by inspection:

$$\begin{cases} A_{1,1} = 0 \\ A_{1,2} = 0 \\ B_1 = 1 \end{cases}$$

Linearizing equation (8) using

$$\begin{cases} P_r = \hat{P}_r + \overline{P}_r \\ Q_{in} = \hat{Q}_{in} + \overline{Q}_{in} \\ Q_{out} = \hat{Q}_{our} + \overline{Q}_{our} \end{cases}$$

yields

$$\begin{split} \frac{d(\hat{P}_r)}{dt} &\approx \frac{\partial \dot{P}_r}{\partial V_{in}} \bigg|_{\overline{P}_r, \overline{V}_{in}, \overline{Q}_{out}} \left(V_{in} - \overline{V}_{in}\right) + \frac{\partial \dot{P}_r}{\partial P_r} \bigg|_{\overline{P}_r, \overline{V}_{in}, \overline{Q}_{out}, \overline{Q}_{out}} \\ &\left(P_r - \overline{P}_r\right) + \frac{\partial \dot{P}_r}{\partial Q_{in}} \bigg|_{\overline{P}_r, \overline{V}_{in}, \overline{Q}_{out}, \overline{Q}_{out}} \left(Q_{in} - \overline{Q}_{in}\right) \\ &+ \frac{\partial \dot{P}_r}{\partial Q_{out}} \bigg|_{\overline{P}_r, \overline{V}_{in}, \overline{Q}_{in}, \overline{Q}_{out}} \left(Q_{out} - \overline{Q}_{out}\right), \end{split}$$

from which we find:

$$egin{cases} A_{2,1} = 0 \ A_{2,2} = -rac{eta}{V_0 - \overline{V}_{in}}rac{\partial \mathcal{Q}_{out}}{\partial P_r}igg|_{P_r = \overline{P}_r}. \ B_2 = rac{eta}{V_0 - \overline{V}_{in}} \end{cases}$$

Equations (11) and (12) both use the term $\frac{\partial Q_{out}}{\partial P_r}\bigg|_{P_r=\overline{P}_r}$, which is defined as:

$$\frac{\partial Q_{out}}{\partial P_r}\bigg|_{P_r = \overline{P}_r} = \frac{a\pi}{b} \left(1 - \frac{2L\tau_0}{\overline{P}_r R} \right)^{1/n} \left(\frac{\overline{P}_r R}{2mL} \right)^{1/n} \tag{15}$$

$$a = 48L^{3}\tau_{0}^{3}n^{3} + 24L^{2}\overline{P}_{r}R\tau_{0}^{2}n^{2} + 6L\overline{P}_{r}^{2}R^{2}\tau_{0}n^{2}$$

$$+ 6L\overline{P}_{r}^{2}R^{2}\tau_{0}n + 2\overline{P}_{r}^{3}R^{3}n^{2} + 3\overline{P}_{r}^{3}R^{3}n + \overline{P}_{r}^{3}R^{3}$$

$$(16)$$

$$b = \overline{P}_r^4 (6n^3 + 11n^2 + 6n + 1). \tag{17}$$

Using equations (15)–(17), term $A_{2,2}$ can be further evaluated to find:

$$A_{2,2} = -\frac{\beta}{V_0 - \overline{V}_{in}} \frac{a\pi}{b} \left(1 - \frac{2L\tau_0}{\overline{P}_r R} \right)^{1/n} \left(\frac{\overline{P}_r R}{2mL} \right)^{1/n}.$$

Using a similar procedure, the linearized output equation used in the linear model is found. Defining the linearization relations and linearizing equation (7) results in equation (18), which may be solved to find equation (19), which is readily solved using the preceding solution.

$$\begin{cases}
P_r = \hat{P}_r + \overline{P}_r \\
Q_{out} = \hat{Q}_{out} + \overline{Q}_{out} \\
\hat{Q}_{out} = \frac{\partial Q_{out}}{\partial P_r} \Big|_{P_r = \overline{P}_r} \hat{P}_r
\end{cases}$$
(18)

$$Q_{out} = \frac{\partial Q_{out}}{\partial P_r} \bigg|_{P_r = \overline{P}_r} \hat{P}_r + \overline{Q}_{out}.$$
(19)

Corresponding author

Andrej Simeunović can be contacted at: simeunovic.1@osu. edu